# Analytical winding loss and inductance models for gapped inductors with Litz or solid wires



**Originally published in:**
IEEE Transactions on Power Electronics 37(12), https://doi.org/10.1109/TPEL.2022.3187155

# Analytical winding loss and inductance models for gapped inductors with Litz or solid wires

Thomas Ewald, *Student Member, IEEE,* Jürgen Biela, *Senior Member, IEEE,*
Email: ewald@hpe.ee.ethz.ch, jbiela@ethz.ch

***Abstract*—In gapped inductors, the fringing field of the air gaps causes additional eddy current losses in the windings and an increase of the inductance. Since this impact of the fringing field is very significant, calculating the additional eddy current losses and the inductance increase is important in the design of inductors. This paper proposes analytical formulas to accurately calculate the inductance and the additional eddy current losses in gapped inductors with solid round wire and Litz wire windings. The analytical formulas are verified by measurements, showing that the proposed models are accurate over a wide frequency range.**

***Index Terms*—Magnetic Components, Inductance, Winding Losses, Magnetic Field, Fringing field**

## I. Introduction

COMMONLY, state of the art inductor design unites comprehensive multiobjective optimization and virtual prototyping, to avoid costly and time-consuming design procedures and redesigns. For this purpose, accurate and fast, and at best analytical models are required for two things, that are particularly important: Calculating the correct inductance value is necessary to ensure the converter system operating at its desired point of operation. In addition, the winding losses determine the size of the component. In case of gapped inductors, the non-homogeneous magnetic field (fringing field) in the core window caused by the air gap(s), has a significant impact on both, the inductance value and the winding losses. This makes it necessary to consider the fringing field in the inductance and winding loss calculation.

Analytical inductance calculation is typically based on magnetic equivalent circuits [1] to consider the impact of a finite permeability and the increasing effective cross-section of the air gap due to the fringing effect. Hereby, considering the air gap fringing field takes place either by empirical correction factors [2]–[5], where general validity is not given, or by the Schwarz-Christoffel (SC) transformation [6], [7]. The SC approaches show increasing errors for larger air gaps, which was already recognized, but not correctly attributed, in [8].

On the other hand, winding loss calculation is based on determining the frequency-dependent eddy current losses [9], [10], which requires a 2D field calculation in case of gapped core windows. This can be performed either with FEM [9], or analytically [11]. Since this paper is focussed on analytical modelling, literature references to numerical, semi-numerical, and empirical models are omitted.

Simple analytical methods, e.g. [12], [13], are not available for gapped core windows. In the case of gapped core windows, the mirroring method is often used to compute the field [14], [15], which in combination with point-wise evaluation of the resulting magnetic field formulation leads to elevated computation times and adds complexity to the model. Analytical expressions are not given. An accurate analytical magnetic field formulation is presented in [16], where a system of coefficients must be solved numerically and numerical integration is used to obtain the losses per individual conductor. However, numerical integration adds significant computational effort to the model and makes implementation complicated. Analytical formulas for the fringing field are given in [17], [18], however, only the fringing field losses are derived based on approximate formulas, whereas the proximity and the skin effect losses are ignored (the question, if the loss components are orthogonal is not addressed). Furthermore, all modelling approaches for winding losses result in 2D per-unit-length losses or inductance values, so an additional length scaling model is necessary to obtain the total losses. In the case of a gapped inductor, considering the 3D geometry is crucial, since the fringing field of the air gaps is locally affecting the winding losses differently.

The first goal of this paper is to derive a comprehensive set of formulas for calculating the winding losses in gapped inductors with solid round or Litz wire, where the skin, the proximity, and the fringing effect are taken into account. This results in closed-form winding loss formulas that are comparable in complexity to known loss models neglecting the fringing field [12], [13]. In contrast to mentioned literatur, this paper proposes formulas for the actual losses by considering the complete inductor geometry, instead of the losses per unit length. The presented formulas are not applicable to foil conductors, because foil conductors act as eddy current shields

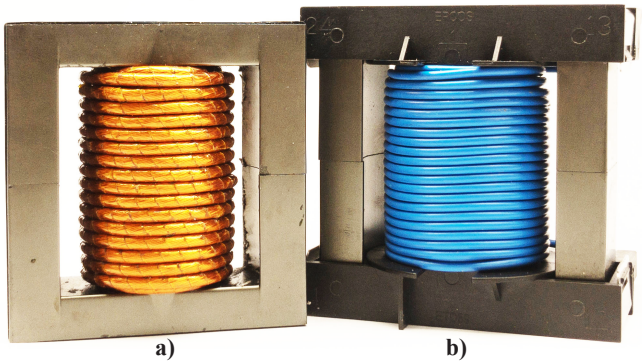

**a)** **b)**

Fig. 1. Inductors wound on an ETD 59/31/22 core **a)** with high-frequency Litz wire and **b)** with solid round wire and an additional coil former.

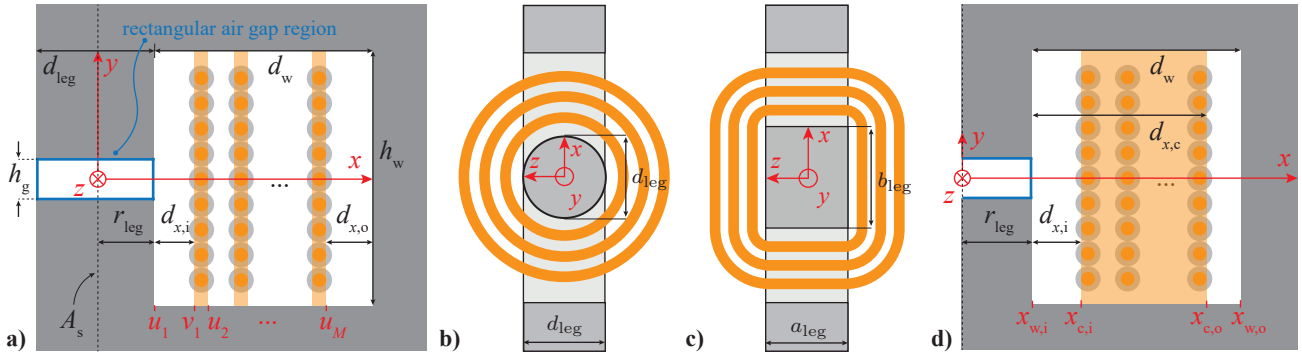


Fig. 2. **a)** 2D core window of an E/ER/ETD type inductor. $A_\mathrm{s}$ is the rotational axis of symmetry. **b)** Top view of a ER/ETD type inductor with circular centre leg used for the derivation of the length scaling. **c)** Top view of a E type inductor with rectangular centre leg. **d)** Simplified 2D core window, considering the whole winding as a unified conductor block.

and must be modelled accordingly [19].

In addition, expressions for the inductance are derived since the magnetic field is analytically calculated. These expressions correctly predict the inductance value of a gapped inductor, where the magnetic energy in the air gap, the core, and the core window (2D fringing field and 1D layer field) are considered. Even though methods for the inductance calculation exist, the models proposed in this paper have notable advantages, since they are physically connected to the Maxwell equations and offer higher accuracy (a comparison with models from literature and a discussion is provided in this paper).

The paper is organized as follows: In sec. II the geometry of the considered inductor is introduced, and geometrical parameters are given. Sec. III-V present analytical formulas for calculating the inductance and the frequency-dependent resistance of gapped inductors. The formulas consider the magnetic fringing field of the air gap(s), which affects both, inductance and resistance. In addition, an extension of the formulas to geometries with rectangular centre legs is proposed in sec. VI. Hereby, the final formulas are provided, which can be implemented directly using the geometrical parameters given in sec. II – the derivations of the equations are moved to the appendix. Finally, sec. VII verifies the model with FEM simulations and measurements performed on two prototype inductors, and discusses the results.

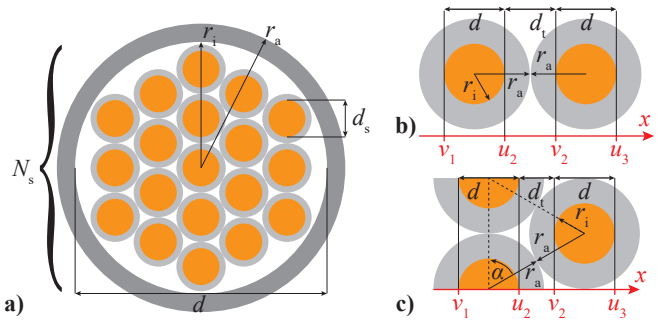


Fig. 3. **a)** Depiction of the cross section of a Litz wire. **b)** Ideal case of a winding arrangement of solid round wires. **c)** Orthocyclic winding arrangement of solid round wires.

## II. Geometry of the Inductor

The inductor that is considered in this paper is an E/ER/ETD type inductor. The core is commercially available and the centre leg is gapped for energy storage.

For modelling purposes, the inductor geometry is separated into a 2D core window (cf. Fig. 2a and d) and the corresponding 1D length scaling, which is determined by the center leg cross section (cf. Fig. 2b and c). The 2D core window is divided into $M = N_\mathrm{EFC}+1$ non-conductive layers (NCR) and $N_\mathrm{EFC}$ equivalent foil conductors (EFC, copper shaded in Fig. 2a), in alternating order. The EFC represent the winding layers, where the winding is either solid round wire or Litz wire. In each individual EFC there are $N_n$ conductors vertically aligned, where $N_n$ is the number of conductors in the $n$-th EFC. From that it follows that the total number of conductors is $N = \sum_{n=1}^{N_\mathrm{EFC}} N_n$. All EFC have the same width $d$ (wich is also the wire diameter), the NCR next to the centre leg (e.g. bobbin) is considered with $d_{x,\mathrm{i}}$, the distances between the conductors are $d_\mathrm{t}$, and the distance between the outermost conductor and the limb is $d_{x,\mathrm{o}}$. Moreover, for a simpler modelling approach, Fig. 2d) shows the 2D core window with a unified conductor block (copper shaded).

The air gaps are considered as separate regions (blue rectangle in Fig. 2a), with the individual height $h_\mathrm{g}$. In case of multiple gaps, $N_\mathrm{g}$ is the number of gaps, which are assumed to be placed evenly along the centre leg surface ($y$-axis) with symmetry to the $x$-axis (cf. app. A).

Fig. 3b) and c) show how to derive the distances $d$ and $d_\mathrm{t}$ for an idealized winding and an orthocyclic winding. In case of the idealized winding, $d = 2r_\mathrm{i}$, and $d_\mathrm{t} = 2(r_\mathrm{a} - r_\mathrm{i})$. In case of an orthocyclic winding, $\alpha$ is 60°. Hence, $d = 2r_\mathrm{i}$, and $d_\mathrm{t} = \sqrt{3}r_\mathrm{a} - 2r_\mathrm{i}$. Here, $r_\mathrm{a}$ and $r_\mathrm{i}$ are the radii of the copper wire with and without insulation, respectively. In case of Litz wire, $d = 2r_\mathrm{i}$ is the diameter of the bundle without outer insulation (cf. Fig. 3a), $d_\mathrm{s}$ is the individual strand diameter, and $N_\mathrm{s}$ is the number of strands in the bundle.

## III. Inductance and Winding Loss Formulas

This section provides analytical formulas to effectivly calculate the increased winding loss caused by the skin, proximity, and fringing effect, as well as the increased inductance due

to the air gap's fringing field. Thereby, the derivations of the different equations are given in the appendix, and referenced in the respective text passage to obtain a compact presentation of the models. The formulas in their presented form are all valid for cores with circular centre legs (ER/ETD), and in sec. VI an extension of the formulas to cores with rectangular centre legs (E) is provided. Two slightly different models are proposed in the following.

The first, called the **compact model**, assumes the winding to be tightly packed (orthocyclic) and the number of conductors to be the same in every EFC, so that the distance between conductive (EFC) and non-conductive layers $d_\mathrm{t}$ becomes zero, and the individual layers can be regarded as a unified conductor (UC, copper shaded in Fig. 2d). This assumption is justified in most applications.

The second model, called **layer model**, derives the magnetic energy and the winding losses for each layer separately. This model yields more accurate results, if there is a significantly larger distance $d_\mathrm{t}$ between the winding layers, which would lead to errors in the compact model. In addition, this model does not assume that the individual layers contain the same number of conductors.

Both models combine a reluctance model for the inductance of the core and the air gap (without fringing) with a model for the magnetic energy in the core window, that is stored in the 2D fringing field. The individual inductances are summed, based on the fact that the inductance depends linearly on the magnetic energy. Thereby, the partial inductance of the air gap (and the core) is (cf. app. B)

$$L_\mathrm{g} = \frac{\mu_0 |k_\mu|^2 N^2}{N_\mathrm{g}^2 h_\mathrm{g}^2} \left( V_\mathrm{g} + \frac{V_\mathrm{e}}{\mu_r^*} \right) \tag{1}$$

where $k_\mu$ is given in (20). For cores with a high relative permeability $k_\mu \approx 1$ results. Note, that the partial inductance of the air gap(s) may be complex, if the relative permeability is complex (cf. app. A). The volume of the gap(s) is

$$V_\mathrm{g} = \frac{\pi d_\mathrm{leg}^2}{4} N_\mathrm{g} h_\mathrm{g} \tag{2}$$

and the volume of the core $V_\mathrm{e}$ is either given, or $V_\mathrm{e} = l_\mathrm{e} A_\mathrm{e}$, where $A_\mathrm{e}$ is the effective core cross-section.

## IV. Compact Model

This model is derived based on Fig. 2d). The 1D magnetic field increases linearly along the $x$-axis in the winding block and is constant everywhere else in the core window. The additional air gap fringing field is modelled with the 2D solution of Maxwell's partial differential equations (PDE) in Cartesian coordinates. This makes it possible to obtain compact analytical formulas for the calculation of the additional fringing inductance and the eddy current losses caused by the fringing field.

### A. Inductance

As mentioned, the total inductance $L$ is determined by summing individual energy contributions, namely of the air gap(s) and the core $L_\mathrm{g}$, and the core window. Hereby, the energy in the core window is theoretically further divided into the energy stored in the fringing field $L_\mathrm{f}$ and the energy in the 1D field between the layers $L_\mathrm{1D}$. The typical contribution of $L_\mathrm{f}$ to the overall inductance value is difficult to quantify, as it strongly depends on the geometry. In [6], [7] it contributes between $6\,\%$ to $41\,\%$. However, the contribution of $L_\mathrm{1D}$ of the 1D layer field is in the low percentage range for a gapped inductor, which makes it justifiable to neglect $L_\mathrm{1D}$. For the sake of completeness, it is derived in app. D and can be added to (3). The total inductance is then

$$L = L_\mathrm{g} + L_\mathrm{f} \tag{3}$$

As shown in app. D, the partial inductance $L_\mathrm{f}$ of the air gap fringing field can be calculated by the formula

$$L_\mathrm{f} = \frac{2\pi h_\mathrm{w}}{\mu_0} \sum_{k=1}^{\infty} c_k(x_\mathrm{w,i}, x_\mathrm{w,o}) |C_k|^2 + d_k(x_\mathrm{w,i}, x_\mathrm{w,o}) |D_k|^2 \tag{4}$$

with $x_\mathrm{w,i}$ and $x_\mathrm{w,o}$ depicted in Fig. 2d),

$$\begin{aligned} C_k &= -\frac{2\mu_0 k_\mu N}{p_k h_\mathrm{w} \left(1 - \mathrm{e}^{-2p_k d_\mathrm{w}}\right)} \operatorname{si}\left(p_k \frac{h_\mathrm{g}}{2}\right) \\ D_k &= C_k \, \mathrm{e}^{-2p_k d_\mathrm{w}} \end{aligned} \tag{5}$$

where $\operatorname{si}(x) = {}^{\sin(x)}\!/_{x}$, $p_k = {}^{2\pi k N_\mathrm{g}}\!/_{h_\mathrm{w}}$, and

$$\begin{aligned} c_k(x_1, x_2) &= \left[ -\frac{\mathrm{e}^{-2p_k(x-u_1)} \left(2p_k x + 1\right)}{4} \right]_{x_1}^{x_2} \\ d_k(x_1, x_2) &= \left[ \frac{\mathrm{e}^{2p_k(x-u_1)} \left(2p_k x - 1\right)}{4} \right]_{x_1}^{x_2} \end{aligned} \tag{6}$$

### B. Resistance of solid round wire

The effective AC resistance of the inductor, as derived in app. E and G, is:

$$R = R_\mathrm{DC} \left( F_R + G_R \frac{L_\mathrm{UC}}{\mu_0 V_\mathrm{UC}} \right) \tag{7}$$

Here,

$$\begin{aligned} L_\mathrm{UC} = {} & \frac{\mu_0 \pi N^2}{h_\mathrm{w}} \frac{x_\mathrm{c,o}^2 + 2x_\mathrm{c,i}x_\mathrm{c,o} - 3x_\mathrm{c,i}^2}{6} \\ & + \frac{2\pi h_\mathrm{w}}{\mu_0} \sum_{k=1}^{\infty} c_k(x_\mathrm{c,i}, x_\mathrm{c,o}) |C_k|^2 + d_k(x_\mathrm{c,i}, x_\mathrm{c,o}) |D_k|^2 \end{aligned} \tag{8}$$

is the partial inductance of the unified conductor block, the coefficients $C_k$ and $D_k$ are given in (5), the functions $c_k$ and $d_k$ are given in (6), and

$$\begin{aligned} F_R &= \frac{1}{2} \operatorname{Re}\left\{ \frac{\alpha \mathrm{I}_0(\alpha)}{\mathrm{I}_1(\alpha)} \right\} \\ G_R &= \pi^2 d^2 \operatorname{Re}\left\{ \frac{\alpha \mathrm{I}_1(\alpha)}{\mathrm{I}_0(\alpha)} \right\} \\ \alpha &= (1 + \mathrm{j}) \frac{d}{2\delta} \end{aligned} \tag{9}$$

are based on [20]. The function $\mathrm{I}_\nu$ is the modified Bessel function of the first kind and the $\nu$-th order. In there, $\delta$, $\omega$,

$\sigma$, and $\mu_0$ are the skin depth, angular frequency, conductivity, and vacuum permeability, respectively. Furthermore,

$$R_{\mathrm{DC}} = \frac{4N\left(x_{\mathrm{c,o}} + x_{\mathrm{c,i}}\right)}{\sigma d^2}$$

is the DC resistance of the winding and

$$V_{\mathrm{UC}} = \pi h_{\mathrm{w}}\left(x_{\mathrm{c,o}}^2 - x_{\mathrm{c,i}}^2\right) \tag{10}$$

is the volume of the unified conductor block (cf. Fig. 2d).

### C. Resistance of Litz wire

In case of Litz wire, the formula for the effective AC resistance of the inductor is (cf. app. H and J):

$$R = R'_{\mathrm{DC}}\left(F'_R + G'_R\left(\frac{L_{\mathrm{UC}}}{\mu_0 V_{\mathrm{UC}}} + \frac{1}{2\pi^2 d^2}\right)\right) \tag{11}$$

with $L_{\mathrm{UC}}$ (8), $C_k$ and $D_k$ (5), $c_k$ and $d_k$ (6). Moreover,

$$\begin{aligned} F'_R &= \frac{1}{2}\,\mathrm{Re}\left\{\frac{\alpha' \mathrm{I}_0(\alpha')}{\mathrm{I}_1(\alpha')}\right\} \\ G'_R &= \pi^2 d_{\mathrm{s}}^2 N_{\mathrm{s}}^2\,\mathrm{Re}\left\{\frac{\alpha' \mathrm{I}_1(\alpha')}{\mathrm{I}_0(\alpha')}\right\} \\ \alpha' &= (1+\mathrm{j})\frac{d_{\mathrm{s}}}{2\delta} \\ R'_{\mathrm{DC}} &= \frac{4N\left(x_{\mathrm{c,o}} + x_{\mathrm{c,i}}\right)}{\sigma d_{\mathrm{s}}^2 N_{\mathrm{s}}} \end{aligned} \tag{12}$$

and $V_{\mathrm{UC}}$ is given in (10).

The compact model typically underestimates the additional losses caused by the fringing field, which is caused by the fact that the magnetic energy between layers is considered in the field averaging. The expected error increases with the insulation distance $d_{\mathrm{t}}$, which makes (7) and (11) only viable for comparatively small insulation distances.

Further note, that in this context app. G and J derive the loss components $R_{1\mathrm{D}}$ and $R_{\mathrm{f}}$ separately, which might be interesting in some applications, and is used in sec. VII to show the impact of the individual components on the total losses of the inductor.

## V. Layer Model

This model is derived based on the geometry in Fig. 2a) and Fig. 3b) & c). The 1D magnetic layer field is assumed to increase linearly inside each EFC, but is constant in the NCR between the EFC. For larger distances $d_{\mathrm{t}}$ this is more accurate, since the non-zero distances have a significant impact on the magnetic field averaging used in this paper, which slightly affects the inductance and can cause significant errors in the resistance calculation with the compact model. The air gap fringing field is modelled with the 2D solution of the Maxwell equations in Cartesian coordinates. However, due to the discontinuous function of the 1D layer field, all formulas must be evaluated per layer, resulting in more complicated formulas.

### A. Inductance

Since with this model the inductane for each layer (NCR and EFC) is described, the inductance is given as the sum of the partial inductances of the air gap(s) (1) and the partial inductances of the individual layers (14), derived in app. C:

$$L = L_{\mathrm{g}} + \sum_{m=1}^{M} L_m^{(\mathrm{NCR})} + \sum_{n=1}^{N_{\mathrm{EFC}}} L_n^{(\mathrm{EFC})} \tag{13}$$

Here, (13) considers the magnetic energy stored in the air gaps, in the fringing field of the air gaps, and in the winding layers, which makes it different than (3), and e.g. [7], where the contribution of the 1D layer field is ignored. The contribution of the partial layer inductances is typically a bit higher than (4). From app. C, the partial inductance of the $m$-th NCR and the $n$-th EFC is:

$$\begin{aligned} L_m^{(\mathrm{NCR})} &= \frac{2\pi h_{\mathrm{w}}}{\mu_0}\left(B_{m,0}^2 d_m\left(\frac{d_m}{2} + u_m\right)\right. \\ &\left. + \sum_{k=1}^{\infty} c_k(u_m, u_m + d_m)|C_k|^2 + d_k(u_m, u_m + d_m)|D_k|^2\right) \\ L_n^{(\mathrm{EFC})} &= \frac{2\pi h_{\mathrm{w}}}{\mu_0}\left(C_{n,0}^2 d^3\left(d + \frac{4v_n}{3}\right)\right. \\ &+ 2C_{n,0}D_{n,0}d^2\left(\frac{2d}{3} + v_n\right) + D_{n,0}^2 d\left(\frac{d}{2} + v_n\right) \\ &\left. + \sum_{k=1}^{\infty} c_k(v_n, v_n + d)|C_k|^2 + d_k(v_n, v_n + d)|D_k|^2\right) \end{aligned} \tag{14}$$

where the functions $c_k$ and $d_k$ are given in (6), and the coefficients $C_k$ and $D_k$ are given in (5), and

$$C_{n,0} = -\frac{\mu_0 N_n}{2dh_{\mathrm{w}}} \qquad D_{n,0} \overset{(n=m)}{=} B_{m,0} = \frac{\mu_0}{h_{\mathrm{w}}}\sum_{i=m}^{N_{\mathrm{EFC}}} N_m$$

The parameter $d_m$ in (14) refers to the width of the $m$-th NCR and is either $d_{x,\mathrm{i}}$, $d_{\mathrm{t}}$, or $d_{x,\mathrm{o}}$.

### B. Resistance of solid round wire

The total effective AC resistance of the inductor, as derived in app. E and F, is:

$$R = \sum_{n=1}^{N_{\mathrm{EFC}}} R_{\mathrm{DC},n}\left(F_R + G_R\frac{L_n^{(\mathrm{EFC})}}{\mu_0 V_n}\right) \tag{15}$$

with $L_n^{(\mathrm{EFC})}$ from (14), $F_R$ and $G_R$ from (9), the DC resistance of the $n$-th layer

$$R_{\mathrm{DC},n} = \frac{4N_n\left(2v_n + d\right)}{\sigma d^2}$$

and its volume

$$V_n = \pi d h_{\mathrm{w}}\left(2v_n + d\right) \tag{16}$$

### C. Resistance of Litz wire

In case of Litz wire, the total effective AC resistance, as derived in app. H and I, is given as

$$R = \sum_{n=1}^{N_{\mathrm{EFC}}} R'_{\mathrm{DC},n}\left(F'_R + G'_R\left(\frac{L_n^{(\mathrm{EFC})}}{\mu_0 V_n} + \frac{1}{2\pi^2 d^2}\right)\right) \tag{17}$$

with $L_n^{(\mathrm{EFC})}$ from (14), $F'_R$ and $G'_R$ from (12), the DC resistance of the $n$-th layer

$$R'_{\mathrm{DC},n} = \frac{4N_n\,(2v_n + d)}{\sigma d_\mathrm{s}^2 N_\mathrm{s}}$$

and its volume $V_n$ given in (16).

## VI. Extension to Rectangular Centre Legs

To consider rectangular centre legs, a different length scaling of the layer is required. In order to make use of the already obtained results from app. C, a coefficient $k_\mathrm{rect}$ is defined, that establishes a relation between the circumferences $C$ of a rectangle and a circle. In the following it is assumed, that the geometry has a rectangular cross-section with width $b_\mathrm{leg} = d_\mathrm{leg}$ and depth $a_\mathrm{leg}$, as given in Fig. 2c). Then,

$$k_\mathrm{rect} = \frac{C_\mathrm{rect}}{C_\mathrm{circ}} = \frac{4}{\pi}\left(1 + \frac{a_\mathrm{leg} - b_\mathrm{leg}}{4r_x}\right)$$

where $r_x$ is the geometric mean radius of the respective layer to the origin (e.g. $r_x = v_1 + {}^{d}/_{2}$ for the first EFC, cf. Fig. 2a). Every layer that is considered in the calculation (NCR and EFC) must be adjusted by its respective coefficient. The coefficients are used to scale the partial inductances of the core window, (4), (8), and (14), and the resistances, (7), (11), (15), and (17). Note, that in the resistance formulas, terms that contain any partial indcutance must not be scaled, to avoid double-scaling. In addition, the volume of the air gap is different for a rectangular centre leg:

$$V_\mathrm{g} = b_\mathrm{leg} a_\mathrm{leg} N_\mathrm{g} h_\mathrm{g}$$

which must be replaced in (1). This procedure was successfully applied and verified in [19].

## VII. Verification

The models are verified in two steps. First, FEM simulations are conducted to show the models accuracy by comparing the analytical derivations with a 2D axis-symmetric FEM model in sec. VII-A. In a second step, measurements are performed with prototype inductors, which are compared to analytical results of the winding losses and the inductance values in sec. VII-B. If not stated otherwise, the layer model is used for verification purposes.

TABLE I
FE Models with Solid Round (FE 1) and Litz Wire (FE 2)

| | FE 1 | FE 2 | | Description |
|---|---|---|---|---|
| | ETD 59/31/22 | ETD 29/16/10 | | Core type |
| $d_{x,\mathrm{i}}$ | 1 | 1 | mm | Dist. centre leg to 1. EFC |
| $h_\mathrm{g}$ | 2 | 2 | mm | Air gap height |
| $N_\mathrm{EFC}$ | 3 | 1 | | # of EFC |
| $N_n$ | 35 | 11 | | # of cond. per EFC |
| $d$ | 0.8 | 1.65 | mm | Cond. thickness |
| $d_\mathrm{t}$ | 0.4 | – | mm | Inter-layer distance |
| $N_\mathrm{s}$ | – | 37 | | # of strands |
| $d_\mathrm{s}$ | – | 0.1 | mm | Strand diameter |

### A. Verification with FEM

The inductance and the resistance factor ${}^{R}/_{R_\mathrm{DC}}$ are studied over a wide frequency range. Two finite element models are set up, one with solid round wire, and one with Litz wire. The geometrical specifications of the FE models are given in Tab. I and are based on commercially available cores. To obtain comparable results, the frequency range for both FE models is adjusted, so that the parameter sweep covers the range of $\Delta$ from 0.1 to 10, where $\Delta = d/\delta$ is the relation of the respective wire/strand diameter to the skin depth. The assumed temperature is 20 °C. Fig. 4 shows the results. The error of the proposed models arising at high frequencies originates from the fact, that the underlying model for the magnetic field in the core window (outside the conductors) neglects any high-frequency effects due to the current displacement in the conductors. However, the magnitude of the error is shown to be comparatively low. The results prove, that the model predicts the losses of the inductor accurate even at high frequencies.

Fig. 4a) compares the proposed inductance models with FEM simulations of inductor 1 (FE 1) from Tab. I. It is shown, that the inductance decreases in FEM simulations at high frequencies. This effect is caused by the inhomogeneous magnetic field inside the conductors, which is not considered in the inductance calculation. This effect is usually negligible in round or Litz wires, since their typical design criterium is $\Delta \leq 1$. However, the overall change of the inductance value at $\Delta = 10$ is $-6.2\,\%$, which is not negligible. A model for the analytical compensation of this effect is retained for future

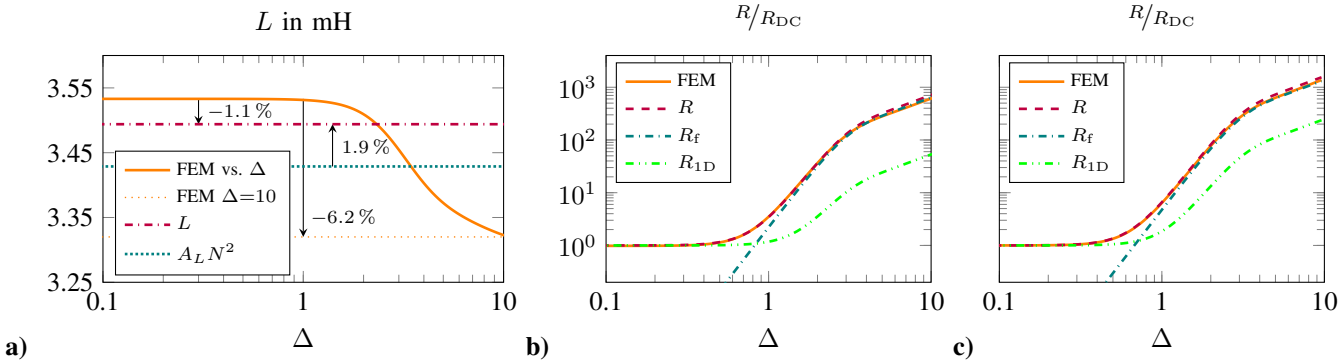


Fig. 4. Comparison of the proposed models with 2D axis-symmetric FEM simulations. **a)** Model FE 1 from Tab. I: $L$ refers to (13), $A_L N^2$ is the inductance according to manufacturer's data. **b)** FE 1 from Tab. I: Resistance factor ${}^{R}/_{R_\mathrm{DC}}$ of the total resistance $R$ (15), and of the partial resistances $R_\mathrm{f}$ (38) and $R_\mathrm{1D}$ (37). The frequency ranges from 66.5 Hz to 665 kHz. **c)** FE 2 from Tab. I: ${}^{R}/_{R_\mathrm{DC}}$ of the total resistance $R$ for Litz wire (17), and the partial resistances $R_\mathrm{f}$ (41) and $R_\mathrm{1D}$ (40). The frequency ranges from 4.26 kHz to 42.6 MHz.

publication.

Fig. 4b) compares the proposed resistance models with FEM simulations of FE 1 from Tab. I. The results show, that the proposed model predicts the winding losses accurately. Nevertheless, since the inductance model overestimates the inductance by neglecting the counteracting effect of the conductor's magnetic field, the resistance model consequently overestimates the winding losses. The maximum error is $14.2\,\%$ at $\Delta = 10$, the average error is $1.8\,\%$. In addition, the partial resistance factors based on the newly proposed fringing field model (38) and the existing 1D model (37) are plotted, to show the individual contributions to the calculation.

Fig. 4c) shows the comparison of the proposed models with FEM simulations of inductor 2 (FE 2) from Tab. I. Here, the maximum error occurs at $\Delta = 5$ and is $14.9\,\%$. The average error is $3.5\,\%$. In addition, the individual contributions are shown with the resistance increase caused by the air gap fringing field (41) and the 1D field assumption (40).

### B. Verification with measurements

Two prototype inductors are made with the commercial core, as specified in Tab. II and shown in Fig. 1, made from Epcos N87 ferrite. Inductor 1 (IND 1) has a solid round wire winding with an additional bobbin, the Litz wire winding of inductor 2 (IND 2) is wound directly around the centre leg without an additional bobbin. The measurements are performed at room temperature. The resistance measurements are done with an impedance analyzer Keysight E4990A. To avoid variations, the impedance analyzer was configured to take the average of five values per frequency point. In addition, multiple frequency sweeps were performed. Regarding measurement accuracy, it can be concluded that the overall measurement error is below 1 % between 1 kHz and 1 MHz, according to the manufacturer's data sheet and the inductor specifications. The inductance is measured with a power choke tester DPG10 from ed-k (step voltage method).

The calculated inductances of both inductors are compared to the measured values given in Tab. III, along with the calculated error. For comparison, the inductance resulting from the $A_L$ value is given, which is very accurate. However, this is not surprising, since the manufacturer measures this value as well. Nevertheless, for custom cores the $A_L$-value is not available. The comparison with (1) shows, that neglecting the fringing field yields significant errors of approximately $-25\,\%$.

TABLE II
INDUCTORS WITH SOLID ROUND (IND 1) AND LITZ WIRE (IND 2)

| | IND 1 | IND 2 | | Description |
|---|---|---|---|---|
| | ETD 59/31/22 | ETD 59/31/22 | | Core type |
| $h_g$ | 2 | 2 | mm | Air gap height |
| $N_{EFC}$ | 3 | 3 | | # of EFC |
| $N_n$ | 21 | 16 | | # of cond. per EFC |
| $d$ | 1 | 2.3 | mm | Conductor (bundle) diameter |
| $N_s$ | – | 60 | | # of strands |
| $d_s$ | – | 0.25 | mm | Strand diameter |
| $C_{res}$ | 29.6 | 42.7 | pF | Measured capacitance |

The stray capacitance of the inductor is determined via a measurement of the first resonant frequency $f_{res} = \omega_{res}/2\pi$ as $C_{res} = 1/(\omega_{res}^2 L)$ (measured with a floating core) and added to the analytical impedance model:

$$Z = \left( (R + \mathrm{j}\omega L)^{-1} + \mathrm{j}\omega C_{res} \right)^{-1} \tag{18}$$

Note, that in the above equation the inductance may be complex (cf. app. A). Then,

$$\mathrm{j}\omega L = \mathrm{j}\omega \left( L' - \mathrm{j}L'' \right) = \mathrm{j}\omega L' + R_c \tag{19}$$

which means, that the imaginary part of the inductance resembles a core loss resistor $R_c = \omega L''$ depending on the frequency and the imaginary part of the relative permeability.

TABLE III
COMPARSION OF CALCULATED AND MEASURED INDUCTANCE VALUES

| Inductor | $L$ meas. | $L$ (13) | $L$ (3) | $L$ (1) | $A_L N^2$ |
|---|---|---|---|---|---|
| IND 1 | 1.23 mH | 1.28 mH | 1.29 mH | 0.92 mH | 1.23 mH |
| (Err.) | – | 3.9 % | 4.0 % | −25.6 % | 0 % |
| IND 2 | 745 µH | 740 µH | 740 µH | 531 µH | 717 µH |
| (Err.) | – | −0.7 % | −0.7 % | −28.7 % | −3.8 % |

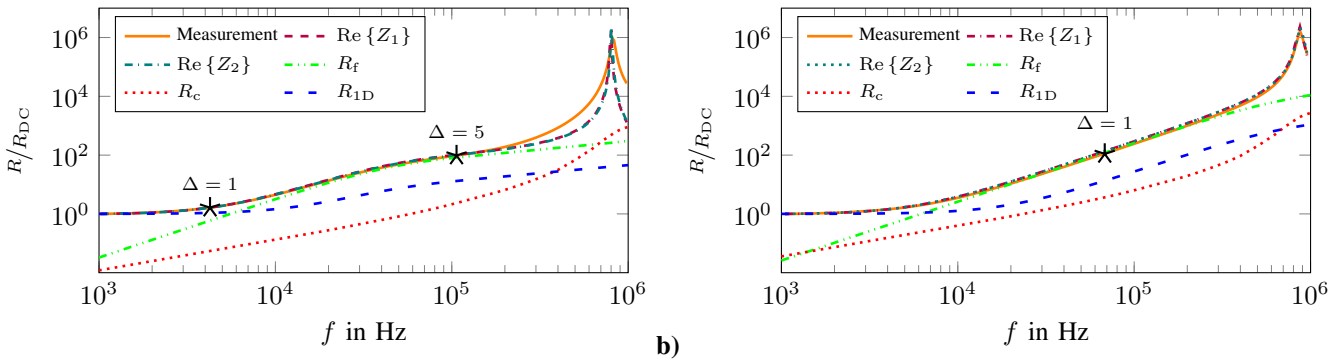


Fig. 5. Comparison of the proposed models with measurements performed with an impedance analyzer. **a)** Calculated resistance factor $R/R_{DC}$ of IND 1: $Z_1$ refers to (18) computed with (13) and (15), $Z_2$ is computed with the compact models (3) and (7), in addition the partial resistances $R_f$ (38) and $R_{1D}$ (37), and $R_c$ (19), which is the core resistor. **b)** $R/R_{DC}$ of IND 2: $Z_1$ is computed with (13) and (17), the compact models (3) and (11) are used to compute $Z_2$, and the partial resistances are calculated using (41), (40), and (19). Note, that the partial resistance $R_{1D}$ is equivalent to models from literature [12], [13], which neglect the presence of an air gap. It is noteable, that the neglection of an air gap results in significant underestimation of the overall resistance increase vs. frequency.

Fig. 5a) compares the calculated resistance factor of IND 1 with the measured values. Up to a relation of the wire diameter and the skin depth of $\Delta = 5$ ($f = 106\,\mathrm{kHz}$), the results match the measurement well. The average error for $\Delta \leq 5$ of (15) is $2.6\,\%$ and the average error of (7) in the same frequency range is $1.2\,\%$.

Fig. 5b) compares the calculated resistance factor of IND 2 with Litz wire to the measured values. Again, the results match well. However, the calculated error is notably higher. The average error of (17) for $\Delta \leq 1$ ($f = 68\,\mathrm{kHz}$) is $9.7\,\%$ and the average error of (11) in the same range is $9.7\,\%$ as well. Note, that the Litz wire winding was assumed to be orthocyclic with comparatively thin outer insulation, which led to a calculated value of $d_\mathrm{t} \approx 0$. Hence, (17) and (11) yield the same results. The error over the full depicted range is $11.9\,\%$.

Overall, the prediction of the effective resistance is very accurate for IND 1 up to 106 kHz ($\Delta = 5$), and the predicted effective resistance of a Litz wire winding (IND 2) is accurate up to at least 68 kHz ($\Delta = 1$). Since Litz wire is specifically used in scenarios where $\Delta < 1$, this proves the model's accuracy. As Fig. 5a) shows a notable deviation above 100 kHz, it needs to be evaluated whether the results can be used to validate the model, which is done in sec. VII-C.

### C. Deviation of measurements and analytical model

Fig. 5a) shows an increased error at frequencies above 100 kHz, which is not reproducible with FEM simulations (cf. sec. VII-A). This leads to the conclusion that this error is caused either by an erroneous capacitance or by miscalculated core losses. Nevertheless, the model can already be considered validated in the frequency range below 100 kHz (cf. sec. VII-B). In the following, the error is examined more closely for the frequency ranges below and above 100 kHz.

Generally, the impedance analyzer predicts the amplitude and phase of the devices under test (DUT) accurately (error less than 1 % according to manufacturer's data sheet, depends on the design). Exceptions might be the frequency range around the resonant frequency (which is not the desired operating point), where the measured current is low (extracted from measurement at res. freq.: 31 µA), and very low frequencies, where the reactive part is comparatively small (below 100 Hz, barely measureable phase angle). The measured values of amplitude and phase must be interpreted physically with an equivalent circuit model. In this paper, this is done according to (18).

The measured resistance is in fact the real part of the measured impedance. It contains the winding loss, core loss, and the capactitance. The capacitance plays a role in the frequency range around the resonant frequency and its influence can be modelled accurately with the measured capacitance $C_\mathrm{res}$. Below 1/10 of the resonant frequency (slightly below 100 kHz in Fig. 5) the capacitance can typically be neglected. Characterization of the core loss is a bit more complicated: An N87 core was selected, which is manufactured to have low core losses below 100 kHz (this can be concluded from the imaginary part of the permeability vs. frequency, cf. Fig. 7). Furthermore, the data sheet of the material gives the core losses at 100 kHz to be around 0.23 W (25 mT, 25 °C) for the core under test. For the DUT (IND 1), a flux density of 25 mT would require an exciting current of 0.66 A, which would lead to expected winding losses of 5.5 W at 100 kHz. Hence, the relation of the core losses to the winding losses is approximately 4 % at 100 kHz. The actual value of the flux density extracted from the measurement is 25 µT (no data is given for such a low excitation in the data sheet). Since the winding losses scale with the squared current, the core losses scale with the squared flux density in first approximation, and current and flux density have a linear relation (assuming no saturation), the relation of winding and core losses should not change for changing excitation. Eventually, it can be concluded that capacitance and core losses can be neglected below a frequency of 100 kHz in case of IND 1.

For frequencies far above 100 kHz, the manufacturer does not provide accurate data for the core losses, and capacitive effects become dominant. Therefore, the frequency range above 100 kHz is not considered for the verification of the model. Eventually, a different method to characterize the total inductor losses in the higher frequency range (above 100 kHz in this case, depending on the material and the DUT specifications) is necessary, since the impedance analyzer measurement misses the opportunity to separate the relevant loss mechanisms. For this purpose, the authors of [21], [22] combine different measurement methods (e.g. the B-H loop measurement [23] for core loss characterization) to separate winding and core losses.

### D. Motivation of the proposed inductance model

Since the proposed inductance models in this paper, i.e. (3) and (13), require more complicated calculations than existing models from literature, it is compared to those models, in order to show that its use will produce more accurate and reliable results. In comparison, simple empirical formulas, e.g. [4], [20], offer a practical and easy to use way to incorporate the air gap fringing paths into the inductance calculation. However, the scope of application of empirical models in terms of geometrical restrictions cannot be defined. This raises the question of the reliability of the results obtained with those models. Physically proven concepts, e.g. [6], [7], have the advantage of having a clear relation to the Maxwell equations. However, it was found that models based on the SC transformation tend to underestimate the reluctance when the air gap becomes larger compared to the core window height and the width of the centre leg. This observation is based on the fact that the magnetic potential on the edge of the ferromagnetic material is assumed to be linear in the derivation of the equations, which is an approximation that depends strongly on the geometrical relations of the centre leg width and height, and the air gap height.

A study was performed, where the proposed model (13) and the models from mentioned literature were compared to a FEM model based on the parameters of Tab. I, but with infinite relative permeability so that the air gap reluctance is simultaneously the overall reluctance. A circular centre leg was assumed, so from [7] the correction factor $\sigma_r$ for circular

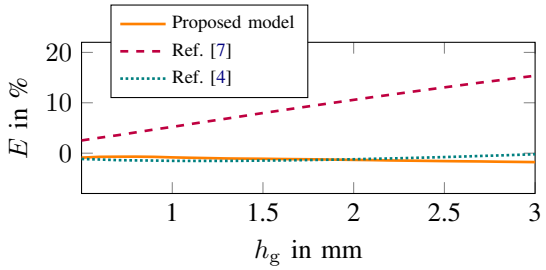


Fig. 6. Relative error of different inductance models compared to an FEM study with infinite relative permeability.

centre legs was used – on the model presented in [4] this has no impact. The results are shown in Fig. 6 as the relative error $E = 100(L/L_{\mathrm{FEM}} - 1)\%$. There, it can be seen that the empirical formula of [4] accurately predicts the inductance for any air gap size. However, as mentioned, formulas of this kind lack the physical derivations, hence, it is not possible to state general validity. The model from [7] shows increasing errors for larger are gap sizes, where the sizes are still well in the range of actually manufactured cores. An error of $15\,\%$ was also reported in [8] for an air gap of $3.18\,\mathrm{mm}$, using [7]. This matches the results from Fig. 6 well. Finally, even though (13) slightly underestimates the inductance, it can be stated that the proposed formula accurately predicts the inductance for any air gap size.

## VIII. Conclusion

This paper derives a detailed analytical model for the magnetic field inside the core window of gapped inductors. The magnetic field model is used to develop analytical models for the inductance and, based on existing models, for the winding losses in solid round wire windings or Litz wire. The resulting formulas allow to predict the increased inductance and winding losses, caused by skin, proximity, and fringing effects, while considering a finite permeability, and cores with circular or rectangular centre legs. The resulting model is capable of predicting the inductance of a prototype inductor within $4\,\%$ and the winding losses within $10\,\%$, which is validated by measurements.

## Appendix A
## Model Derivation in Cartesian Coordinates

In the following, derivations for a closed-form formulation of the magnetic field in the core window are presented. The analytical solution is obtained by directly solving the Maxwell equations. The following assumptions are applied:

1) The core material is ideal: $\mu_r \to \infty$
2) Magneto-quasi-static calculations: $\nabla \times \vec{H} = \vec{J}$
3) Harmonic time dependency: $\mathrm{d}/\mathrm{d}t \to \mathrm{j}\omega$
4) The core window is infinitly long in $z$-direction
5) The current density in the conductors is spatially constant

Note, that assumption 1) is applied only while solving the PDE in the core window, otherwise the permeability is taken into account, cf. Eq. (20). Furthermore, assumption 4) is applied for deriving the 2D fields, and later dropped for the quasi-3D integration of the fields around the circumference of the soleniodal winding. Note, that the magnetic field in the core window is assumed to be unaffected by the eddy currents in the conductors. This is a necessary assumption to obtain analytical solutions. An iterative procedure to incorporate the interactions between magnetic field and eddy currents is described for example in [10].

The magnetic field strength in the air gap, for a ferromagnetic core material with finite permeability $\mu_\mathrm{r}$, is:

$$H_\mathrm{g} = k_\mu \frac{N\hat{I}}{N_\mathrm{g} h_\mathrm{g}} \quad \text{with} \quad k_\mu = \frac{1}{1 + \frac{l_\mathrm{e}}{\mu_\mathrm{r} N_\mathrm{g} h_\mathrm{g}}} \tag{20}$$

where it is assumed that the average magnetic flux densities, in the core and inside the air gaps respectively, are the same and spatially constant (only a $y$-component, independent of the position). Here, the effective magnetic path length $l_\mathrm{e}$ is known (either given by the manufacturer or calculated accordingly [24]).

In (20), the relative permeability of the core may be complex. In that case $\mu_\mathrm{r} = \mu_\mathrm{r}' - \mathrm{j}\mu_\mathrm{r}''$ [25], where $\mu_\mathrm{r}'$ and $\mu_\mathrm{r}''$ are the real and the imaginary part of the complex permeability. Fig. 7 shows the complex permeability as a function of the frequency for the material N87. In case of a complex relative permeability, the inductance becomes complex:

$$L = L' - \mathrm{j}L''$$

where $L'$ and $L''$ are the real and imaginary part of the inductance.

The magnetic field and flux density in the core window depend on the position $(x, y)$. The current, the current density, and the magnetic potential are defined to have only components in $z$-direction, since they are perpendicular to the magnetic field. The magnetic potential is obtained by solving the Laplace and the Poisson equation in the NCR and in the EFC:

$$\nabla^2 \vec{A}^{(\mathrm{NCR})} = 0 \qquad \nabla^2 \vec{A}^{(\mathrm{EFC})} = -\mu_0 J_n \tag{21}$$

where $J_n = N_n \hat{I}/(d h_\mathrm{w})$ is the spatially constant current density of the $n$-th EFC. Expressions for the magnetic potential

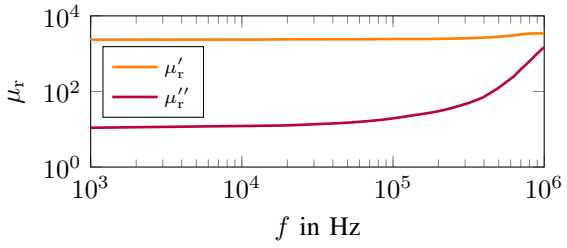


Fig. 7. Real and imaginary part, $\mu_\mathrm{r}'$ and $\mu_\mathrm{r}''$ respectively, of the complex permeability of the material N87, extracted from the manufacturer's data sheet for $B = 25\,\mathrm{mT}$ (small signal excitation) and $T = 25\,^\circ\mathrm{C}$.

that satisfy (21) in the $m$-th NCR and the $n$-th EFC are:

$$\begin{aligned} A_{z,m}^{(\mathrm{NCR})} &= B_{m,0}\hat{I}(x-u_m) \\ &\quad + \sum_{k=1}^{\infty}\left(C_k\,\mathrm{e}^{-p_k(x-u_1)} + D_k\,\mathrm{e}^{p_k(x-u_1)}\right)\hat{I}\cos(p_k y) \\ A_{z,n}^{(\mathrm{EFC})} &= C_{n,0}\hat{I}(x-v_n)^2 + D_{n,0}\hat{I}(x-v_n) \\ &\quad + \sum_{k=1}^{\infty}\left(C_k\,\mathrm{e}^{-p_k(x-u_1)} + D_k\,\mathrm{e}^{p_k(x-u_1)}\right)\hat{I}\cos(p_k y) \end{aligned} \tag{22}$$

where $u_m$ and $v_n$ denote the $x$-references of the respective layer, so that $u_1 = d_{\mathrm{leg}}/2$ (cf. Fig. 2). The magnetic potential is composed of two components: The terms indicated by 0 represent the magnetic field and satisfy the Laplace/Poisson equation in the respective layer, as well as Ampere's law for an air gap in the centre leg and ideal core material (the MMF is absorbed by the air gap). The sum terms indicated by $k$ satisfy the Laplace equation. To satisfy Ampere's law, magnetic field's $y$-component on the boundary between air gap(s) and core window is assumed to be (20) and is used as boundary condition to solve the PDE inside the rectangular core window. This procedure is already used in the literature [16], [26].

The flux density components for the NCR and the EFC are calculated with $\vec{B} = \nabla\times\vec{A}$:

$$\begin{aligned} B_x &= -\sum_{k=1}^{\infty} p_k\left(C_k\,\mathrm{e}^{-p_k(x-u_1)} + D_k\,\mathrm{e}^{p_k(x-u_1)}\right)\hat{I}\sin(p_k y) \\ B_{y,m}^{(\mathrm{NCR})} &= -B_{m,0}\hat{I} \\ &\quad + \sum_{k=1}^{\infty} p_k\left(C_k\,\mathrm{e}^{-p_k(x-u_1)} - D_k\,\mathrm{e}^{p_k(x-u_1)}\right)\hat{I}\cos(p_k y) \\ B_{y,n}^{(\mathrm{EFC})} &= -\left(2C_{n,0}(x-v_n) + D_{n,0}\right)\hat{I} \\ &\quad + \sum_{k=1}^{\infty} p_k\left(C_k\,\mathrm{e}^{-p_k(x-u_1)} - D_k\,\mathrm{e}^{p_k(x-u_1)}\right)\hat{I}\cos(p_k y) \end{aligned} \tag{23}$$

The expressions for the magnetic field (23) are used in the following to derive the necessary coefficients, based on Gauss's law, which states that the magnetic field and the flux density must be continuous at adjacent boundaries, if the relative permeability is the same in both layers. This is approximately true for air and any conductive, non-ferromagnetic material (e.g. copper).

To satisfy the boundary conditions of the magnetic flux density $B_x(x,-h_{\mathrm{w}}/2) = B_x(x,h_{\mathrm{w}}/2) = 0$, it follows, that

$$p_k = \frac{2\pi k N_{\mathrm{g}}}{h_{\mathrm{w}}}$$

Since eq. (23) for the $y$-component of the flux density must satisfy Ampere's law for an arbitrary number of $k$ (also zero), the coefficient $B_{m,0}$ for the $m$-th NCR is given as:

$$B_{m,0}\hat{I} = \frac{\mu_0\hat{I}}{h_{\mathrm{w}}}\sum_{i=m}^{N_{\mathrm{EFC}}} N_m \quad\Rightarrow\quad B_{m,0} = \frac{\mu_0}{h_{\mathrm{w}}}\sum_{i=m}^{N_{\mathrm{EFC}}} N_m$$

where $\hat{I}$ is the peak amplitude of the sinusoidal current. Substituting (22) into (21) directly yields:

$$C_{n,0}\hat{I} = -\frac{\mu_0 J_n}{2} \quad\Rightarrow\quad C_{n,0} = -\frac{\mu_0 N_n}{2dh_{\mathrm{w}}}$$

Lastly, the solution for the coefficients $D_{n,0}$ is obtained with the fact, that the $y$-component of the flux density at the boundary of the $m$-th NCR and the $n$-th EFC ($n=m$, $x=v_n$) must be continuous:

$$D_{n,0} \overset{(m=n)}{=} B_{m,0}$$

The spatial coefficients (indicated by $k$) are obtained by solving the boundary value problem (core window) in rectangular coordinates. The air gap field (20), which is known at the boundary between the air gap and core window, is decomposed into a Fourier series, as shown in [16] and [27]. This yields

$$\begin{aligned} \left(C_k - D_k\right)\hat{I} &= -\frac{2\mu_0 k_\mu N\hat{I}}{p_k h_{\mathrm{w}}}\,\mathrm{si}\left(p_k\frac{h_{\mathrm{g}}}{2}\right) \\ \left(C_k\,\mathrm{e}^{-p_k d_{\mathrm{w}}} - D_k\,\mathrm{e}^{p_k d_{\mathrm{w}}}\right)\hat{I} &= 0 \end{aligned} \tag{24}$$

where $\mathrm{si}(x) = {}^{\sin(x)}/_{x}$. Reformulating (24) yields:

$$\begin{aligned} C_k &= -\frac{2\mu_0 k_\mu N}{p_k h_{\mathrm{w}}\left(1-\mathrm{e}^{-2p_k d_{\mathrm{w}}}\right)}\,\mathrm{si}\left(p_k\frac{h_{\mathrm{g}}}{2}\right) \\ D_k &= C_k\,\mathrm{e}^{-2p_k d_{\mathrm{w}}} \end{aligned}$$

## Appendix B
## Partial Air Gap Inductance

The partial inductance of the air gap (including the core), neglecting any fringing, is derived from the magnetic energy that is stored in the gap (and the core), and the volume of the gaps (and the core). In case of a finite permeability, which may also be complex, $\mu_{\mathrm{r}}$ denotes the relative permeability of the core. Then, the partial inductance is:

$$L_{\mathrm{g}} = \frac{V_{\mathrm{g}}B_{\mathrm{g}}H_{\mathrm{g}}^*}{\hat{I}^2} + \frac{V_{\mathrm{e}}B_{\mathrm{c}}H_{\mathrm{c}}^*}{\hat{I}^2} = \frac{\mu_0}{\hat{I}^2}|H_{\mathrm{g}}|^2\left(V_{\mathrm{g}} + \frac{V_{\mathrm{e}}}{\mu_r^*}\right) \tag{25}$$

where $H$ is the magnetic field strength, $B$ is the magnetic flux density, $V$ is the volume, and $\hat{I}$ is the current (amplitude value). Moreover, the index g denotes variables associated with the air gap(s), and the index c denotes variables of the core. It is assumed that $B_{\mathrm{g}} = \mu_0 H_{\mathrm{g}}$, $B_{\mathrm{c}} = B_{\mathrm{g}}$, and $H_{\mathrm{c}}^* = {}^{B_{\mathrm{c}}^*}/_{\mu_0\mu_{\mathrm{r}}^*}$. Furthermore, $V_{\mathrm{g}}$ is given in (2) and the core volume $V_{\mathrm{e}}$ is assumed to be known. Substituting (20) into (25) yields (1). Hereby, the magnetic field in the air gap(s) is assumed to be homogeneous and constant, thus independent of the $(x,y)$-position inside the air gap region (cf. Fig. 2a).

## Appendix C
## Partial Magnetic Layer Energy and Inductance

For the calculation of the magnetic energy, an accurate length scaling for each layer is used, according to Fig. 2b):

$$W = \frac{1}{2\mu_0}\iiint x\;|\vec{B}|^2\;\mathrm{d}x\;\mathrm{d}y\;\mathrm{d}z \tag{26}$$

For this purpose, the coordinate system is changed to polar coordinates and the integration in $z$-direction is replaced by integration along the circumference (note $x$ in the integrand).

With (23), the analytical expressions of the magnetic flux density in the $m$-th NCR and in the $n$-th EFC are given. Performing the integration yields the magnetic energy in the $m$-th NCR and the $n$-th EFC, respectively:

$$W_m^{(\mathrm{NCR})} = \frac{\pi h_\mathrm{w} \hat{I}^2}{\mu_0}\left(B_{m,0}^2 d_m\left(\frac{d_m}{2}+u_m\right) + \sum_{k=1}^{\infty} c_k(u_m, u_m+d_m)|C_k|^2 + d_k(u_m, u_m+d_m)|D_k|^2\right)$$

$$W_n^{(\mathrm{EFC})} = \frac{\pi h_\mathrm{w} \hat{I}^2}{\mu_0}\left(C_{n,0}^2 d^3\left(d+\frac{4v_n}{3}\right) + 2C_{n,0}D_{n,0}d^2\left(\frac{2d}{3}+v_n\right) + D_{n,0}^2 d\left(\frac{d}{2}+v_n\right) + \sum_{k=1}^{\infty} c_k(v_n, v_n+d)|C_k|^2 + d_k(v_n, v_n+d)|D_k|^2\right)$$

Here, the parameter $d_m$ refers to the width of the $m$-th NCR and is either $d_{x,\mathrm{i}}$, $d_\mathrm{t}$, or $d_{x,\mathrm{o}}$, the coefficients $C_k$ and $D_k$ are given in (5), and the functions $c_k(x_1, x_2)$ and $d_k(x_1, x_2)$ are given in (6). There, the coordinates $x_1$ and $x_2$ enclose the considered layer, with $x_2 > x_1$, and the origin of the core window $u_1$, defined according to Fig. 2. The partial layer inductance is

$$L = \frac{2W}{\hat{I}^2} \tag{27}$$

eventually leading to (14).

An important finding here is, that the contributions of the 1D layer field and the 2D air gap fringing field to the magnetic energy are separated in the end result (the terms indicated by 0 and the infinite sum indicated by $k$), because all terms containing an integral along $y$-direction over $\cos(p_k y)$, $\sin(p_j y)\sin(p_k y)$, or $\cos(p_j y)\cos(p_k y)$ vanish in the integration over $y$ in the limits from $-h_\mathrm{w}/2$ to $h_\mathrm{w}/2$, due to the orthogonality of the trigonometric functions. This means that these contributions can be considered separately, e.g. by two separate formulas:

$$W = W_{1\mathrm{D}} + W_\mathrm{f} \tag{28}$$

where $W_{1\mathrm{D}}$ and $W_\mathrm{f}$ denote the 1D layer field and the 2D air gap fringing field, respectively.

## Appendix D
## Separated Layer and Fringing Inductances

As shown in the previous section, the magnetic energy, and therefore the partial inductance caused by the 1D layer field and the air gap fringing field are separable. Hence, the magnetic energy in the core window $W_\mathrm{f}$, that is caused by the 2D fringing field, is:

$$W_\mathrm{f} = \frac{\pi h_\mathrm{w} \hat{I}^2}{\mu_0}\sum_{k=1}^{\infty} c_k(x_{\mathrm{w,i}}, x_{\mathrm{w,o}})|C_k|^2 + d_k(x_{\mathrm{w,i}}, x_{\mathrm{w,o}})|D_k|^2 \tag{29}$$

where the functions $c_k$ and $d_k$, given in (6), consider the $x$-dimension of the complete core window. Substituting (29) into (27) eventually leads to (4).

Since (29) considers the 2D air gap fringing field, but not the 1D layer field, the magnetic energy of the latter one is calculated additionally as:

$$W_{1\mathrm{D}} = \frac{\mu_0}{2}\frac{\pi N^2 \hat{I}^2}{h_\mathrm{w}}\left(\frac{x_{\mathrm{c,o}}^2}{6} + \frac{x_{\mathrm{c,i}}x_{\mathrm{c,o}}}{3} + \frac{x_{\mathrm{c,i}}^2}{2} - x_{\mathrm{w,i}}^2\right) \tag{30}$$

where (31) and (32) are added, which consider the magnetic energy contributions from the UC, and the NCR between the centre leg and the UC. The 1D magnetic field between the UC and the outer limb is zero, hence, no magnetic energy from the field is stored there. The individual contributions are derived as follows: A 1D magnetic flux density is assumed in the UC ($d_\mathrm{t} = 0$) in Fig. 2d), which is defined according to (23), where the $x$-dependent 1D magnetic flux density is given as:

$$B_y^{(\mathrm{UC})} = \frac{\mu_0 N \hat{I}}{h_\mathrm{w}}\left(\frac{x - x_{\mathrm{c,i}}}{x_{\mathrm{c,o}} - x_{\mathrm{c,i}}} - 1\right)$$

Calculating the magnetic energy according to (26) yields

$$W^{(\mathrm{UC})} = \frac{\mu_0}{2}\frac{\pi N^2 \hat{I}^2}{h_\mathrm{w}}\frac{x_{\mathrm{c,o}}^2 + 2x_{\mathrm{c,i}}x_{\mathrm{c,o}} - 3x_{\mathrm{c,i}}^2}{6} \tag{31}$$

Furthermore, again using (23), the $x$-independent 1D magnetic flux density in the NCR between centre leg and the UC is given as

$$B_y^{(\mathrm{NCR})} = -\frac{\mu_0 N \hat{I}}{h_\mathrm{w}}$$

Hence, the energy contribution $W_\mathrm{NCR}$ of the NCR between centre leg and the UC, using again (26), is:

$$W^{(\mathrm{NCR})} = \frac{\mu_0}{2}\frac{\pi N^2 \hat{I}^2}{h_\mathrm{w}}\left(x_{\mathrm{c,i}}^2 - x_{\mathrm{w,i}}^2\right) \tag{32}$$

The inductance $L_{1\mathrm{D}}$ caused by the 1D layer field is then given by substituting (30) into (27).

## Appendix E
## Effective AC Resistance Calculation

In the following, the effective AC resistance is calculated based on formulas from [20], which results in models comparable to known models [12], [13]. A general formula for the power loss of a round conductor carrying a sinusoidal current $\hat{I}$ (amplitude), and exposed to a spatially homogeneous external magnetic field $\hat{H}_\mathrm{ext}$ of the same frequency, is:

$$P = \frac{\hat{I}^2}{\sigma\pi d^2}\,\mathrm{Re}\left\{\frac{\alpha \mathrm{I}_0(\alpha)}{\mathrm{I}_1(\alpha)}\right\} + \frac{2\pi\hat{H}_\mathrm{ext}^2}{\sigma}\,\mathrm{Re}\left\{\frac{\alpha \mathrm{I}_1(\alpha)}{\mathrm{I}_0(\alpha)}\right\} \tag{33}$$

where $\mathrm{I}_\nu$ is the modified Bessel function of the first kind of order $\nu$, $\sigma$ is the conductivity of the material, $d$ is the diameter of the wire, and $\alpha$ is given in (9). Formula (33) can be rewritten in terms of the DC resistance of the wire $R_\mathrm{DC} = 4/\sigma\pi d^2$, such that

$$P = \frac{1}{2}R_\mathrm{DC}F_R\hat{I}^2 + \frac{1}{2}R_\mathrm{DC}G_R\hat{H}_\mathrm{ext}^2 \tag{34}$$

where $F_R$ and $G_R$ are unitless factors to take into account the additional losses caused by the skin effect and an external magnetic field $\hat{H}_\mathrm{ext}$ (proximity losses), both given in (9). The squared external magnetic field amplitude $\hat{H}_\mathrm{ext}^2$ can be expressed in terms of its *spatial* r.m.s. value $\hat{H}_\mathrm{rms}^2$, that can

be derived from the stored magnetic energy in a volume of consideration in the core window:

$$\hat{H}_{\mathrm{ext}}^2 = \hat{H}_{\mathrm{rms}}^2 = \frac{L_{\mathrm{p}}\hat{I}^2}{\mu_0 V_{\mathrm{p}}} \tag{35}$$

where $V_{\mathrm{p}}$ is the considered volume and $L_{\mathrm{p}}$ is its partial inductance. Substituting (35) into (34), and dividing the result by ${\hat{I}^2}/{2}$ (r.m.s. value of the current) yields a compact expression for the effective AC resistance:

$$R = R_{\mathrm{DC}}\left(F_R + G_R\frac{L_{\mathrm{p}}}{\mu_0 V_{\mathrm{p}}}\right) \tag{36}$$

## Appendix F
## AC Resistance – Layer Model

The expressions for the partial magnetic energy of each layer, previously obtained in app. C, are substituted into (27) to obtain the partial inductance $L_n^{(\mathrm{EFC})}$ of the $n$-th EFC, given in (14). Substituting the partial inductance into (36) results in the resistance of the $n$-th EFC:

$$R_n = R_{\mathrm{DC},n}\left(F_R + G_R\frac{L_n^{(\mathrm{EFC})}}{\mu_0 V_n}\right)$$

where $R_{\mathrm{DC},n}$ is the DC resistance of the respective layer and $V_n$ is its volume. Eventually, the sum over all $N_{\mathrm{EFC}}$ EFC yields the total resistance of the inductor, leading to (15).

## Appendix G
## AC Resistance – Compact Model

In app. C it is shown, that the magnetic energy contributions of the 1D layer field and of the 2D fringing field can be split into two components: The energy stored in the 1D field $W_{1\mathrm{D}}$ and the energy stored in the 2D fringing field of the air gap(s) $W_{\mathrm{f}}$ (28). Moreover, if it is assumed that the winding is tightly packed (orthocyclic) and the number of conductors is the same in every EFC, the individual layers can be regarded as a unified conductor (UC, copper shaded in Fig. 2d). App. D derives compact formulas for the magnetic energy contributions for $W_{\mathrm{UC}}$ and $W_{\mathrm{f}}$ under these assumptions. Substituting the respective terms of the magnetic energy into (36) yields

$$R = \underbrace{R_{\mathrm{DC}}\left(F_R + G_R\frac{2}{\mu_0}\frac{W_{\mathrm{UC}}}{V_{\mathrm{UC}}\hat{I}^2}\right)}_{R_{1\mathrm{D}}} + \underbrace{R_{\mathrm{DC}}G_R\frac{2}{\mu_0}\frac{W_{\mathrm{f}}}{V_{\mathrm{UC}}\hat{I}^2}}_{R_{\mathrm{f}}}$$

where $R_{\mathrm{DC}}$ is the DC resistance of the winding and $V_{\mathrm{UC}}$ is the volume of the unified conductor block (cf. Fig. 2d). The separable loss component $R_{1\mathrm{D}}$, caused by the skin effect and the external 1D magnetic layer field, is considered by

$$R_{1\mathrm{D}} = R_{\mathrm{DC}}\left(F_R + G_R\frac{\pi N^2}{h_{\mathrm{w}}}\frac{x_{\mathrm{c,o}}^2 + 2x_{\mathrm{c,i}}x_{\mathrm{c,o}} - 3x_{\mathrm{c,i}}^2}{6V_{\mathrm{UC}}}\right) \tag{37}$$

which is equivalent to known 1D models for solid round wire, e.g. [12]. Here, (31) is used for $W_{1\mathrm{D}}$ to obtain the compact formula for the effective inductor resistance, neglecting the air gap fringing field. The formula for the effective AC resistance caused by the air gap fringing field, using (29), is then:

$$R_{\mathrm{f}} = R_{\mathrm{DC}}G_R\frac{2\pi h_{\mathrm{w}}}{\mu_0^2 V_{\mathrm{UC}}} \sum_{k=1}^{\infty} c_k(x_{\mathrm{c,i}}, x_{\mathrm{c,o}})|C_k|^2 + d_k(x_{\mathrm{c,i}}, x_{\mathrm{c,o}})|D_k|^2 \tag{38}$$

Note, that here the functions $c_k$ and $d_k$ consider the core window area from $x_{\mathrm{c,i}}$ to $x_{\mathrm{c,o}}$ (copper shaded layer in Fig. 2d). Eventually, this leads to the total effective AC resistance of the inductor presented in (7).

## Appendix H
## Effective AC Resistance – Litz Wire

A comprehensive survey and comparison of winding loss models for Litz wire can be found in [28]. There, it is shown that an additional loss term must be added to (33) to consider the internal proximity effect of the Litz wire. An expression for the total losses caused by the skin, external, and internal proximity effect, can be derived in a similar way as for solid round wire. It is made use of the fact, that internal and external proximity effects are orthogonal [13], hence:

$$\hat{H}_{\mathrm{ext}}^2 = \hat{H}_{\mathrm{rms}}^2 + \hat{H}_{\mathrm{int}}^2$$

Then, the squared averaged internal magnetic field, which is the same for all wires, is given as:

$$\hat{H}_{\mathrm{int}}^2 = \frac{4}{d^2\pi}\iint_{\mathcal{A}} r H_i^2(r)\ \mathrm{d}\mathcal{A} = \frac{\hat{I}^2}{2\pi^2 d^2}$$

Additionally, formula (33) must be adapted to Litz wire, which consists of $N_{\mathrm{s}}$ strands of the much thinner individual diameter $d_{\mathrm{s}}$, bundled together (cf. Fig. 3a). The power loss of an individual strand is

$$P_{\mathrm{s}} = \frac{\hat{I}'^2}{\sigma\pi d_{\mathrm{s}}^2}\,\mathrm{Re}\left\{\frac{\alpha'\mathrm{I}_0(\alpha')}{\mathrm{I}_1(\alpha')}\right\} + \frac{2\pi\hat{H}_{\mathrm{ext}}^2}{\sigma}\,\mathrm{Re}\left\{\frac{\alpha'\mathrm{I}_1(\alpha')}{\mathrm{I}_0(\alpha')}\right\}$$

where $\alpha'$ is adjusted for the Litz wire strand diameter, according to (12). Note, that the current through each strand is $\hat{I}' = {\hat{I}}/{N_{\mathrm{s}}}$, since the individual strands are connected in parallel. The losses of the bundle are $P = N_{\mathrm{s}}P_{\mathrm{s}}$. Then, with the DC resistance of the Litz wire (bundle) $R'_{\mathrm{DC}} = {4}/{N_{\mathrm{s}}\sigma\pi d_{\mathrm{s}}^2}$, the power loss is again given as

$$P = \frac{1}{2}R'_{\mathrm{DC}}F'_R\hat{I}^2 + \frac{1}{2}R'_{\mathrm{DC}}G'_R\left(\hat{H}_{\mathrm{rms}}^2 + \hat{H}_{\mathrm{int}}^2\right)$$

with $F'_R$ and $G'_R$ given in (12). Finally, following the same step as in app. E, the effective AC resistance for Litz wire is

$$R = R'_{\mathrm{DC}}\left(F'_R + G'_R\left(\frac{L_{\mathrm{p}}}{\mu_0 V_{\mathrm{p}}} + \frac{1}{2\pi^2 d^2}\right)\right) \tag{39}$$

## Appendix I
## AC Resistance – Layer Model – Litz Wire

The effective AC resistance of Litz wire is obtained from (39), where the partial inductance of the layer is obtained the same way as in the previous section, app. F, for solid round wire. Hence,

$$R_n = R'_{\mathrm{DC},n}\left(F'_R + G'_R\left(\frac{L_n^{(\mathrm{EFC})}}{\mu_0 V_n} + \frac{1}{2\pi^2 d^2}\right)\right)$$

with the volume of the respective layer $V_n$ and the DC resistance of the $n$-th Litz wire layer $R'_{\mathrm{DC},n}$. As for solid round wire, the sum over all $N_{\mathrm{EFC}}$ EFC yields the total resistance of the inductor, leading to (17).

## APPENDIX J
## AC RESISTANCE – COMPACT MODEL – LITZ WIRE

In case of Litz wire, the same steps are performed as in app. G, but (39) is used as a starting point. This results in

$$R_{1\mathrm{D}} = R'_{\mathrm{DC}}\left(F'_R + G'_R\left(\frac{1}{2\pi^2 d^2} + \frac{\pi N^2}{h_{\mathrm{w}}}\frac{x_{\mathrm{c,o}}^2 + 2x_{\mathrm{c,i}}x_{\mathrm{c,o}} - 3x_{\mathrm{c,i}}^2}{6V_{\mathrm{UC}}}\right)\right) \quad (40)$$

which is then equivalent to 1D models for Litz wire, e.g. [13], [29], and the impact of the air gap fringing field

$$R_{\mathrm{f}} = R'_{\mathrm{DC}}G'_R\frac{2\pi h_{\mathrm{w}}}{\mu_0^2 V_{\mathrm{UC}}} \sum_{k=1}^{\infty} c_k(x_{\mathrm{c,i}}, x_{\mathrm{c,o}})|C_k|^2 + d_k(x_{\mathrm{c,i}}, x_{\mathrm{c,o}})|D_k|^2 \quad (41)$$

The effective AC resistance of the inductor is the sum of both presented in (11), where $R'_{\mathrm{DC}}$ is the DC resistance of the Litz winding and $V_{\mathrm{UC}}$ is the volume of the winding.

## ACKNOWLEDGMENT

The authors would like to express their acknowledgment to the Baechli AG, Switzerland, and Innosuisse, Switzerland (Appl. No.: 32328.1 IP-ENG), for providing financial support for this project.

## REFERENCES

[1] J. Cale, S. D. Sudhoff, and Li-Quan Tan, "Accurately modeling EI core inductors using a high-fidelity magnetic equivalent circuit approach," *IEEE Transactions on Magnetics*, vol. 42, no. 1, pp. 40–46, Jan. 2006.

[2] A. Van den Bossche, V. Valchev, and T. Filchev, "Improved approximation for fringing permeances in gapped inductors," in *Record of the 37th Industry Applications Conf.* IEEE, 2002.

[3] E. Stenglein and M. Albach, "The reluctance of large air gaps in ferrite cores," in *18th European Conf. on Power Electronics and Applications (EPE ECCE Europe)*. IEEE, Sep. 2016.

[4] C. McLyman, *Transformer and Inductor Design Handbook*. CRC Press, 2017.

[5] A. F. Hoke and C. R. Sullivan, "An improved two-dimensional numerical modeling method for e-core transformers," in *APEC. Seventeenth Annual IEEE Applied Power Electronics Conference and Exposition (Cat. No.02CH37335)*, vol. 1, 3 2002.

[6] A. Balakrishnan, W. T. Joines, and T. G. Wilson, "Air-gap reluctance and inductance calculations for magnetic circuits using a schwarz-christoffel transformation," *IEEE Transactions on Power Electronics*, vol. 12, no. 4, pp. 654–663, July 1997.

[7] J. Muehlethaler, J. W. Kolar, and A. Ecklebe, "A novel approach for 3d air gap reluctance calculations," in *8th International Conference on Power Electronics (ECCE Asia)*, May 2011.

[8] I. Kovačević-Badstübner, R. Burkart, C. Dittli, J. W. Kolar, and A. Musing, "A fast method for the calculation of foil winding losses," in *17th European Conf. on Power Electronics and Applications (EPE ECCE Europe)*, Sep. 2015.

[9] C. R. Sullivan, "Computationally efficient winding loss calculation with multiple windings, arbitrary waveforms, and two-dimensional or three-dimensional field geometry," *IEEE Transactions on Power Electronics*, vol. 16, no. 1, pp. 142–150, Jan. 2001.

[10] M. Albach, "Two-dimensional calculation of winding losses in transformers," in *31st Annu. Power Electronics Specialists Conf.* IEEE, Jun. 2000.

[11] M. Albach and H. Rossmanith, "The influence of air gap size and winding position on the proximity losses in high frequency transformers," in *2001 IEEE 32nd Annual Power Electronics Specialists Conference (IEEE Cat. No.01CH37230)*. IEEE, 2001.

[12] J. A. Ferreira, "Improved analytical modeling of conductive losses in magnetic components," *IEEE Transactions on Power Electronics*, vol. 9, no. 1, pp. 127–131, Jan 1994.

[13] J. Ferreira, "Analytical computation of AC resistance of round and rectangular litz wire windings," *IEE Proceedings B (Electric Power Applications)*, vol. 139, no. 1, p. 21, 1992.

[14] J. Muehlethaler, J. W. Kolar, and A. Ecklebe, "Loss modeling of inductive components employed in power electronic systems," in *8th Int. Conf. Power Electronics*, May 2011, pp. 945–952.

[15] D. Leuenberger and J. Biela, "Accurate and computationally efficient modeling of flyback transformer parasitics and their influence on converter losses," in *17th European Conference on Power Electronics and Applications (EPE ECCE Europe)*. IEEE, Sep. 2015.

[16] P. Wallmeier, N. Frohleke, and H. Grotstollen, "Improved analytical modeling of conductive losses in gapped high-frequency inductors," in *33rd IEEE Industry Applications Society Conf. (IAS)*, vol. 2, Oct. 1998, pp. 913–920.

[17] W. A. Roshen, "Fringing field formulas and winding loss due to an air gap," *IEEE Transactions on Magnetics*, vol. 43, no. 8, pp. 3387–3394, Aug. 2007.

[18] A. V. den Bossche and V. C. Valchev, "Improved calculation of winding losses in gapped inductors," *Journal of Applied Physics*, vol. 97, no. 10, May 2005.

[19] T. Ewald and J. Biela, "Frequency-dependent inductance and winding loss model for gapped foil inductors," *Transactions on Power Electronics*, 2022.

[20] M. Albach, *Induktivitäten in der Leistungselektronik*. Springer Vieweg, Wiesbaden, 2017.

[21] Y. Han, G. Cheung, A. Li, C. R. Sullivan, and D. J. Perreault, "Evaluation of magnetic materials for very high frequency power applications," in *Power Electronics Specialists Conference*. IEEE, jun 2008.

[22] S. Mukherjee, Y. Gao, and D. Maksimovic, "Reduction of AC winding losses due to fringing-field effects in high-frequency inductors with orthogonal air gaps," *Transactions on Power Electronics*, vol. 36, no. 1, pp. 815–828, jan 2021.

[23] J. Muehlethaler, J. Biela, J. W. Kolar, and A. Ecklebe, "Core losses under the dc bias condition based on steinmetz parameters," *IEEE Transactions on Power Electronics*, vol. 27, no. 2, 2 2012.

[24] E. Snelling, *Soft ferrites: properties and applications*. Newnes-Butterworth, 1969.

[25] M. Kazimierczuk, *High Frequency Magnetic Components*. John Wiley & Sons, Ltd, 2013.

[26] T. Ewald and J. Biela, "Analytical eddy current loss model for foil conductors in gapped cores," *23th European Conference on Power Electronics and Applications (EPE ECCE Europe)*, Oct. 2021.

[27] W. F. Trench, "Elementary differential equations," *Faculty Authored and Edited Books and CDs*, no. 8, 2013.

[28] Q. Meng, "Survey and comparison of different 1D and 2D analytical models of HF losses in Litz Wire," in *22nd European Conference on Power Electronics and Applications (EPE ECCE Europe)*, Sep. 2020.

[29] M. Bartoli, N. Noferi, A. Reatti, and M. Kazimierczuk, "Modelling litz-wire winding losses in high-frequency power inductors," in *27th Power Electronics Specialists Conf. (PESC)*. IEEE, 1996.

**Thomas Ewald** (Student Member, IEEE) studied electrical engineering with focus on Energy Conversion Technology at Technical University of Munich (TUM) in Germany. He received his B.Sc. and M.Sc. degree from TUM in 2015 and 2018, respectively. In 2017, he wrote his Master's Thesis at BMW AG in the R&D department for electrical drive components. In his Master's thesis he developed an analytical model for simulating transient processes in both, permanent magnet and electrically excited synchronous machines. Since November 2019 he is a Ph.D. student at the Laboratory for High Power Electronic Systems (HPE) at ETH Zurich, working on analytical inductor models and automated optimization processes.

**Jürgen Biela** (Senior Member, IEEE) received the Diploma (hons.) degree from Friedrich-Alexander Universität Erlangen-Nürnberg, Erlangen, Germany, in 1999, and the Ph.D. degree from the Swiss Federal Institute of Technology (ETH), Zürich, Switzerland, in 2006. In 2000, he joined the Research Department, Siemens A&D, Erlangen, and in 2002, he joined the Power Electronic Systems Laboratory, ETH Zürich, as a Ph.D. Student focusing on electromagnetically integrated resonant converters, where he was a Postdoctoral Fellow from 2006 to 2010. Since 2010, he has been an Associate Professor, and since 2020, a Full Professor of high-power electronic systems with ETH Zurich.